Profiles of high-order moments of longitudinal velocity explained by the random sweeping decorrelation hypothesis

Kelly Y. Huang and Gabriel G. Katul

Phys. Rev. Fluids **7**, 044603 — Published 19 April 2022

DOI: 10.1103/PhysRevFluids.7.044603

Profiles of high-order moments of longitudinal velocity explained by the random sweeping decorrelation hypothesis

Kelly Y. Huang*
Mechanical and Aerospace Engineering, Princeton University, Princeton, NJ, United States and now at Civil and Environmental Engineering and Earth Sciences, University of Notre Dame, Notre Dame, IN, United States

Gabriel G. Katul
Department of Civil and Environmental Engineering, Duke University, Durham, NC, United States
(Dated: April 1, 2022)

Under the assumptions that the random sweeping decorrelation hypothesis applies and that the velocity statistics are near Gaussian, the logarithmic variation of high-order moments of longitudinal velocity with distance from a boundary in the inertial region (where the logarithmic law holds for the mean longitudinal velocity) is explained by the existence of a -1 power law in the longitudinal velocity spectrum. During the Idealized horizontal Planar Array study for Quantifying Surface heterogeneity (IPAQS), measurements and profiles of longitudinal velocity were collected within the first meter from the surface under mild atmospheric thermal stratification. These measurements show good agreement to the proposed theory. Further investigation into the validity of the random sweeping decorrelation hypothesis reveals that it is not strictly valid across all scales but can be viewed as operationally viable due to inherent cancellation in its interaction terms. More importantly, deviations from the random sweeping decorrelation hypothesis predictions appear consistent across the logarithmic region and captured by a quasi-constant, suggesting possible avenues for correction in the modeling of high-order moments.

I. INTRODUCTION

Arguably, one of the most well-known universal features of high Reynolds number wall-bounded turbulence is the logarithmic law [1–3] that describes the profile of the mean longitudinal velocity with vertical distance z from a solid boundary in the inertial or logarithmic region,

$$\frac{\overline{u}}{u_*} \equiv \overline{u}^+ = \frac{1}{\kappa}\ln(z^+) + B, \tag{1}$$

where u is the streamwise velocity, overline denotes ensemble averaging (approximated by time averaging), the $+$ superscript denotes normalization by the friction (or shear) velocity u_* and kinematic viscosity ν, κ is the von Kármán constant, and B is a constant that varies with surface roughness but is assumed to be a constant for smooth surfaces. Ample empirical evidence have supported this log-scaling as reviewed elsewhere [4, 5].

In canonical wall-bounded flows, a logarithmic law for the variance of streamwise velocity $\overline{u'^2}$ coexists in the same region, proposed by Townsend [6] and many others [3, 7] as

$$\overline{u'^2}^+ = B_1 - A_1\ln\left(\frac{z}{\delta}\right), \tag{2}$$

where $\overline{u'^2}^+ = \overline{u'^2}/u_*^2$ is the normalized longitudinal velocity variance, δ is an outer length scale (i.e. the boundary layer thickness or the pipe radius in canonical boundary layer flows), and B_1 and A_1 are similarity constants. This scaling has been theorized based on a number of similarity arguments (e.g. attached eddy hypothesis) and solutions to spectral budget models [6–10], and supported by numerous experimental studies [3, 11–14]. Experiments have shown that the constant A_1 may vary with Reynolds number [15, 16] and approaches ≈ 1.25 [3, 4, 7, 17] at high Reynolds numbers, while B_1 is dependent upon flow conditions and geometry and thus not expected to be universal.

Whether high-order statistics $\overline{u'^{2p}}^+ = \overline{u'^{2p}}/u_*^{2p}$ also scale with $\ln(z/\delta)$ has been a recent subject of study given its relevance in evaluating large-eddy simulation sub-grid modeling and post-processing [18], and in the synthetic generation of turbulence in wind energy design that indicates a need to consider moments more complicated than the

* yhuang28@nd.edu

standard deviation [19]. Meneveau and Marusic [20] proposed that when u' assumes a Gaussian distribution and the eddies are non-interacting,

$$(\overline{u'^{2p}}^{+})^{1/p} = B_p - A_p \ln\left(\frac{z}{\delta}\right), \tag{3}$$

where $p \geq 1$ is the moment order, $A_p = A_1\left[(2p-1)!!\right]^{1/p} = A_1\left[\pi^{-1/2}2^p\Gamma(p+1/2)\right]^{1/p}$, and $\Gamma(\cdot)$ is the gamma function.

Recently, Katul et al. [21] showed that this generalized logarithmic law in high-order moments of longitudinal velocity can be explained by a combination of the random sweeping decorrelation hypothesis (RSDH) and a k_x^{-1} power-law scaling in the near-universal shape of the energy spectrum of the longitudinal velocity $E_u(k_x)$ between $\delta^{-1} \leq k_x \leq z^{-1}$, where k_x is the streamwise wavenumber. The premise is that when the u' statistics are approximately Gaussian and the RSDH holds (where the turbulent eddies are non-interacting and remain undistorted), then the high-order moments of the longitudinal velocity ($p > 1$) can be related to $E_u(k_x)$ (for $p = 1$). Katul et al. [21] examined data from a single sampling height above a uniform ice sheet under near-neutral conditions to investigate the assumptions required for the RSDH, and found that the hypothesis is not strictly valid but can be viewed as operationally viable. However, this work did not evaluate predictions by Eq. 3.

Here, high frequency (0.1 kHz) multi-level near-surface ($z \leq 1$ m) longitudinal velocity data acquired above the salt flats of Utah are used to examine the link between $E_u(k_x)$ and predictions from Eq. 3 across the logarithmic layer. A unique feature of the experiment here is that the -1 power law persists in $E_u(k_x)$ as a result of the proximity to the ground while maintaining very high Reynolds numbers. Further, the theory proposed in Katul et al. [21] is extended to explore its applicability across weakly stratified conditions by allowing the intersection of the -1 and $-5/3$ spectral scaling ranges to shift with atmospheric stability. This shift would account for cases where effects of the thermal stratification result in a change of the eddy size characterizing the break point between the -1 and the $-5/3$ power law scaling, but are not strong enough to introduce different coherent structures that would alter the k_x^{-1} scaling in $E_u(k_x)$.

Overall, good agreement between measured and predicted $\overline{u'^{2p}}^{+}$ from the RSDH was seen for the data analyzed, suggesting that the proposed expression from Katul et al. [21] is an acceptable hypothesis even for the atmospheric surface layer where non-neutral stability conditions prevail. Namely, the model appeared to be able to predict A_p well under the thermal stratification considered, but failed to capture B_p under near-neutral conditions for higher moments and under unstable conditions for all moments. To investigate this deviation and the underlying theory, inherent assumptions of the RSDH were examined in detail in physical space. While violations of the RSDH assumption were observed, inherent compensatory effects similar to those examined in Katul et al. [21] seem to explain the functional utility of the RSDH. Further investigations reveal more or less consistent deviations from the RSDH across the logarithmic layer that could be modeled and corrected for. Notably, at scales larger than $\approx 60z$, the RSDH appears to be applicable but with a constant offset, and at scales bounded by z and $\approx 60z$, the deviations of the measured data from the RSDH prediction can be captured by a quasi-constant $A_m^{1/m}$ that appears to be insensitive to thermal stratification.

II. THEORY

A. Random Sweeping Decorrelation Hypothesis (RSDH)

The RSDH dates back to Tennekes [22], who investigated the relation between the Eulerian and the Lagrangian velocity frequency spectra, and assumed that small eddies (those at least one order of magnitude smaller than the energy-containing eddies) are transported or 'swept' past a Eulerian observer by the energy-containing eddies without any dynamical distortion. As mentioned by Tennekes, this picture is analogous to Taylor's frozen field hypothesis, which suggests that turbulent eddies are advected by the mean streamwise velocity without changes to their properties [23]; the distinction here is that the transport of the small scales is related to the energy content of the larger eddies under the RSDH, as opposed to the mean flow. Tennekes found that if this 'sweeping' occurs, then the large-scale advection gives the dominant contribution to kinetic energy in the inertial subrange; that is, motion in the smaller scales is a result of the kinetic energy of the larger scales. Under this framework, the kinetic energy per unit mass of the larger scales $\overline{u_i'^2}$, where the subscripts $i = 1, 2, 3$ denote the longitudinal, lateral, and vertical directions, respectively, should also be a relevant parameter in the dimensional analysis of the inertial subrange in the Eulerian framework, in addition to the mean turbulent kinetic energy dissipation rate $\overline{\epsilon}$ and wavenumber k (or equivalently frequency f) as proposed by Kolmogorov [24]. Thus, the Eulerian frequency spectra of any velocity component $u_i'^2$ may be described

as

$$E_{u_i}^{(2)}(k) = \alpha_i \bar{\epsilon}^{2/3} \overline{u_i'^2} k^{-5/3}, \tag{4}$$

where α_i is an unknown constant and $\int_0^\infty E_{u_i}^{(2)}(k)\,dk = \overline{u_i'^4}$ is the power spectrum of order 2.

A similar problem was also studied by Dutton and Deaven [25], who investigated the extension of Kolmogorov's dimensional arguments [26] to spectra of algebraic powers of velocity fluctuations:

$$\overline{(u_i^p - \overline{u_i^p})^2} = \overline{u_i^{2p}} - \overline{u_i^p}^2 = \int_{-\infty}^{+\infty} E_{u_i}^{(p)}(k)\,dk, \tag{5}$$

where $E_{u_i}^{(p)}(k)$ is the power spectrum of order p. Dutton and Deaven suggested that if Kolmogorov's dimensional arguments in the inertial subrange [26] also hold for high-order spectra, then

$$E_{u_i}^{(p)}(k) = C_p \bar{\epsilon}^{2p/3} k^{-(2p+3)/3}, \tag{6}$$

where C_p are constants to be determined (with C_1 being the Kolmogorov constant). That is, $E^{(1)} \sim k^{-5/3}$, $E^{(2)} \sim k^{-7/3}$, $E^{(3)} \sim k^{-3}$, etc. From high-order spectra up to $p = 4$ for all velocity components measured at four different elevations above the land surface (in the atmospheric surface layer, the atmospheric boundary layer, and for clear air turbulence conditions), they found that the high-order spectra appear to follow a $-5/3$ power law regardless of p, a significant departure from the predictions of Eq. 6, suggesting that the inertial subrange behavior is defined by more than only $\bar{\epsilon}$ and k.

Motivated by the results of Dutton and Deaven [25], Van Atta and Wyngaard [27] assumed Gaussian statistics for u_i' and found that for the inertial subrange

$$E_{u_i}^{(p)}(k) = \alpha(p) \overline{u_i'^2}^{p-1} E_{u_i}(k), \tag{7}$$

where $\alpha(p) = p^2 \times 1 \times 3 \times 5 \times \ldots \times (2p-3)$. In other words, when the u_i' statistics are approximately Gaussian and the RSDH holds, the high-order spectrum $E_{u_i}^{(p)}(k)$ (for $p \geq 2$) is dependent on the sweeping effect ($\overline{u_i'^2}$) and the first order spectrum $E_{u_i}(k)$ (where $p = 1$). Specifically, the scaling coefficient $\alpha(p)$ arises from Gaussian statistics, while the scaling law itself is dictated by the sweeping. That is, non-Gaussian effects would manifest as a shift to the scaling coefficients but not the law itself. Atmospheric turbulence measurements taken over the ocean appear to confirm Eq. 7 [27].

B. Extension to High-Order Moments

As in Katul et al. [21], the high-order statistics for the longitudinal velocity $\overline{u'^{2p}} = \int_0^\infty E_u^{(p)}(k)\,dk + \overline{u'^p}^2$ are interpreted with the RSDH (Eq. 7) to give

$$\overline{u'^{2p}} = \alpha(p) \left[\overline{u'^2}\right]^{p-1} \int_0^\infty E_u(k)\,dk + \overline{u'^p}^2. \tag{8}$$

For Gaussian statistics, it can be shown that the term $\overline{u'^p}^2$ is identically zero for odd p, and has a value of $\frac{\Gamma((1+p)/2)^2}{\sqrt{\pi}\Gamma(1/2+p)} \overline{u'^{2p}}$ for even p. Thus, the term $\overline{u'^p}^2$ can be absorbed as a corrective coefficient

$$\gamma(p) = \begin{cases} 1 & \text{for odd } p \\ \left(1 - \frac{\Gamma((1+p)/2)^2}{\sqrt{\pi}\Gamma(1/2+p)}\right)^{-1} & \text{for even } p \end{cases} \tag{9}$$

such that Eq. 8 becomes

$$\overline{u'^{2p}} = \gamma(p)\alpha(p) \left[\overline{u'^2}\right]^{p-1} \int_0^\infty E_u(k)\,dk, \tag{10}$$

so that the high-order moments ($p > 1$) now depend on the sweeping velocity and the integral of the first order longitudinal velocity energy spectrum. (Note that for even p, $\gamma(p)$ approaches 1 from its $p = 2$ value of $3/2$ by roughly 2^{-p} as p increases, so that contributions from the $\overline{u'^p}^2$ diminishes raipdly and are negligible by $p = 4$.)

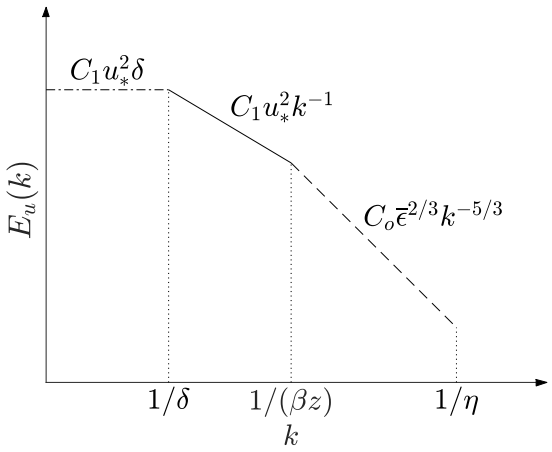

FIG. 1. Illustration depicting the idealized shape and scaling regimes of the model spectrum for $E_u(k)$. The coefficient β is used to account for any shifting due to thermal stratification of the break point between the k^{-1} and $k^{-5/3}$ scaling regions. Continuity at $1/(\beta z)$ then defines $C_1 = C_o \kappa^{-2/3} \beta^{2/3}$. It is to be noted that $\overline{u'^{2p}}$ depends on the integrated spectrum thereby making it less sensitive to non-smooth transitions between scaling regimes.

To arrive at an analytic expression, consider a simplified shape as illustrated in Fig. 1 for $E_u(k)$. This idealized model spectrum is similar to that assumed in Katul et al. [21], which has been found to be a solution to spectral budget models [8, 10, 28, 29]. Here, the intersection between the -1 and $-5/3$ scaling regions is taken to occur at a scale βz, where β is a constant needed to account for variations that could arise due to thermal stratification. Distinguished by three length scales: δ, βz, and the Kolmogorov microscale $\eta = (\nu^3/\overline{\epsilon})^{1/4}$, this model spectrum is described by the following regions:

- $E_u(k) = C_1 u_*^2 \delta$ for $0 \leq k \leq 1/\delta$. This relation is chosen following the reasoning of Katul et al. [21] given the uncertainty in the scaling laws that govern this region and the simplicity of this scaling.
- $E_u(k) = C_1 u_*^2 k^{-1}$ for $1/\delta \leq k \leq 1/(\beta z)$. For near-neutral conditions, this scaling exists for $1/\delta \leq k \leq 1/z$ ($\beta = 1$) as predicted originally by Tchen [30, 31] and by others (e.g. attached eddy hypothesis of Townsend [6]).
- $E_u(k) = C_o \overline{\epsilon}^{2/3} k^{-5/3}$ for $1/(\beta z) \leq k \leq 1/\eta$ in accordance with Kolmogorov scaling [26], where $C_o = (18/55) C_\kappa \approx 0.5$ and $C_\kappa = 1.55$ are empirically determined coefficients [32].

Under the assumption that production $\mathcal{P}$ balances dissipation $\overline{\epsilon}$ at any z and when Eq. 1 holds, $d\overline{U}/dz = u_*/(\kappa z)$ so that $\mathcal{P} = \overline{\epsilon} = u_*^2 d\overline{U}/dz = u_*^3/(\kappa z)$. Combining this estimate for $\overline{\epsilon}$ and continuity at $k = 1/(\beta z)$ then defines $C_1 = C_o \kappa^{-2/3} \beta^{2/3}$ so that the model spectrum is completely defined by u_*, β, and established constants κ and C_κ. Under near-neutral conditions, $\beta = 1$.

Integration of this model spectrum results in

$$\int_0^\infty E_u(k)\, dk = \overline{u'^2} = \int_0^{1/\delta} C_1 u_*^2 \delta\, dk + \int_{1/\delta}^{1/(\beta z)} C_1 u_*^2 k^{-1}\, dk + \int_{1/(\beta z)}^{1/\eta} C_o \overline{\epsilon}^{2/3} k^{-5/3}\, dk. \tag{11}$$

Integrating, substituting $\overline{\epsilon} = u_*^3/\kappa z$, and normalizing by u_*^2 gives

$$\frac{\overline{u'^2}}{u_*^2} \equiv \overline{u'^2}^+ = C_1 \left[1 - \ln\left(\frac{\beta z}{\delta}\right)\right] + \frac{3}{2} C_1 \left[1 - \left(\frac{\eta}{\beta z}\right)^{2/3}\right], \tag{12}$$

which can be reduced to the form of Eq. 2 when

$$A_1 = C_1 \tag{13}$$

and

$$B_1 = A_1 \left[\frac{5}{2} - \frac{3}{2}\left(\frac{\eta}{z}\right)^{2/3} \beta^{-2/3} - \ln(\beta)\right] \tag{14}$$

With $Re_* = z^+ = zu_*/\nu$, B_1 can also be expressed as

$$B_1 = A_1 \left[\frac{5}{2} - \frac{3}{2} \frac{\kappa^{1/6}}{Re_*^{1/2}} \beta^{-2/3} - \ln(\beta) \right]. \tag{15}$$

As $Re_* \to \infty$ under neutral conditions (i.e. $\beta = 1$), $A_1 \approx 0.9$ and $B_1 \approx 2.25$ with $\kappa = 0.4$. Meneveau and Marusic obtained $A_1 = 1.19$ and $B_1 = 1.71$ by fitting Eq. 2 to measured $\overline{u'^2}^+$ at $Re_* \approx 1500$. As summarized and discussed in Katul et al. [21], although not identical, this value of A_1 compares reasonably (within 20%) to C_1 obtained independently from a number of other experiments [28, 33–36], which ranged from $C_1 = 0.9 - 1.1$.

Equation 10 can then be written as

$$\overline{u'^{2p}} = \gamma(p)\alpha(p)\overline{u'^2}^{p-1} u_*^2 \left[B_1 - A_1 \ln\left(\frac{z}{\delta}\right) \right], \tag{16}$$

where again $\alpha(p)$ and $\gamma(p)$ can be defined for Gaussian statistics and does not vary with z, and B_1 and A_1 are defined as functions of C_1 (which is in turn defined as a function of β and well-known constants κ and C_o) following Eqs. 13 and 15. That is, the logarithmic scaling in high-order moments $\overline{u'^{2p}}$ can be explained by a combination of the RSDH and the logarithmic law for the streamwise turbulence intensity $\overline{u'^2}$, which was shown to be a consequence of a k^{-1} scaling in the longitudinal velocity spectrum $E_u(k)$.

Finally, $(\overline{u'^{+2p}})^{1/p}$ can be estimated from Eq. 16 by further substituting $\overline{u'^2} = u_*^2 \left[B_1 - A_1 \ln(z/\delta) \right]$, normalizing by u_*^{2p}, and raising to a power of $1/p$:

$$(\overline{u'^{2p}}^+)^{1/p} = \gamma(p)^{1/p}\alpha(p)^{1/p} \left[B_1 - A_1 \ln\left(\frac{z}{\delta}\right) \right] \tag{17}$$

so that this expression has the same form as Eq. 3 with $B_p = \gamma(p)^{1/p}\alpha(p)^{1/p}B_1$ and $A_p = \gamma(p)^{1/p}\alpha(p)^{1/p}A_1$.

The validity of Eq. 17 within the logarithmic layer will be tested with data measured within one meter above the salt flats of Utah under varying thermal stratification. Due to the measurements' proximity to the ground, the thermal stratification is not expected to deviate significantly from neutral conditions so that the measured spectra should follow the ideal shape assumed in Fig. 1, allowing for direct application of the presented theory that includes the β parameter.

C. Evaluation of the Random Sweeping Decorrelation Hypothesis

To investigate the validity of the RSDH, it is convenient to conduct the analysis in physical rather than spectral space using the high-order structure functions as discussed by Praskovsky et al. [37]. The high-order structure function $D_u^m(r)$ is defined as

$$D_u^m(r) = \overline{[u'^m(x+r) - u'^m(x)]^2}, \tag{18}$$

where r is the separation distance along x, in accordance with Dutton and Deaven [25] (note that this is different than the traditional nth order structure function defined as $D_{u,n}(r) = \overline{(u'(x+r) - u'(x))^n}$).

By using the velocity difference $\Delta u = u'(x+r) - u'(x)$ to replace $u'(x+r)$ in Eq. 18 and expanding,

$$\begin{aligned} D_u^m(r) &= \overline{[(u' + \Delta u)^m - u'^m)]^2} \\ &= m^2 \overline{u'^{2m-2}\Delta u^2} + m^2(m-1)\overline{u'^{2m-3}\Delta u^3} \\ &\qquad + m^2(m-1)\frac{1}{12}(7m-11)\overline{u'^{2m-4}\Delta u^4} + \ldots \end{aligned} \tag{19}$$

If the RSDH is valid, then the large scale and inertial range scales are statistically independent, i.e. smaller eddies experience advective 'sweeping' by the larger eddies with no dynamical distortion. Then, with u' a characteristic velocity for the large scale eddy motion and Δu for the inertial subrange eddy motion, under the RSDH, quantities involving $\overline{u'^k \Delta u^l}$ reduce to $\overline{u'^k}\ \overline{\Delta u^l}$ for $k > 1$ and $l > 1$ so that for $m > 2$,

$$D_u^m = m^2 \overline{u'^{2m-2}}\ \overline{\Delta u^2}\ \Omega\left(m, \overline{u'^k}, \overline{\Delta u^l}\right), \tag{20}$$

where

$$\Omega\left(m, \overline{u'^k}, \overline{\Delta u^l}\right) = 1 + (m-1)\frac{\overline{u'^{2m-3}}}{\overline{u'^{2m-2}}}\frac{\overline{\Delta u^3}}{\overline{\Delta u^2}} + \ldots. \tag{21}$$

Praskovsky et al. [37] showed that for fine-scale turbulence (with small r) at sufficiently high Re, $\Omega(\cdot) \approx 1$ so that Eq. 20 reduces to $D_u^m = m^2 \overline{u'^{2m-2}}\ \overline{\Delta u^2}$. This suggests that the scaling laws describing $D_u^m(r)$ in the inertial subrange are set by not only $\bar{\epsilon}$ and r (used in defining $\overline{\Delta u^2}$ in accordance with Kolmogorov [26]), but also the large-scale energy content $\overline{u'^{2m-2}}$, consistent with the essence of the RSDH.

The scale-wise application of the RSDH can be investigated with two measures as introduced by Praskovsky et al. [37]. One is a measure that directly follows Eq. 20 and the definition of $\Omega(\cdot)$ by normalizing $D_u^m(r)$. The resulting expression,

$$d^m(r) = \frac{D_u^m(r)}{m^2 \overline{u'^{2m-2}}\ \overline{[u'(x+r) - u'(x)]^2}}, \tag{22}$$

will be a direct measure of whether there is sufficiently high Re and separation between the large and small scales. Since $\Omega(\cdot) \to 1$ in this limit, plotting $d^m(r)$ will show the range of validity of the RSDH for the different stability regimes, moment order m, and separation r. As discussed, if the RSDH is valid across all scales, then $d^m(r) = 1$ at all r. Compared to $D_u^m(r)$, the measure $d^m(r)$ is less sensitive to distortions introduced by Taylor's frozen field hypothesis as such distortions will affect both the numerator and the denominator of Eq. 22.

Another measure proposed by Praskovsky et al. [37] is

$$g^m(r) = \frac{1}{m^2 \overline{u'^{2m-2}}} \overline{\left\{ \frac{[u'^m(x+r) - u'^m(x)]^2}{[u'(x+r) - u'(x)]^2} \right\}}. \tag{23}$$

Unlike $d^m(r)$, the measure $g^m(r)$ is not directly related to the problem at hand but the same assumptions leading to $d^m(r) = 1$ also leads to $g^m(r) = 1$ [37]. Since there is only one averaging operation in $g^m(r)$, it will not be affected in the same way by distortions introduced by the usage of Taylor's frozen turbulence hypothesis as $d^m(r)$.

The measures $d^m(r)$ and $g^m(r)$ will be used to examine the validity of the RSDH across the measured dataset at all sampled heights and under all stability conditions. Although $d^m(r) = 1$ and $g^m(r) = 1$ are expected at all scales if the RSDH holds, any absence of significant r dependence (i.e. if $d^m(r)$ and $g^m(r)$ approach a constant $\neq 1$) implies that $\Omega(\cdot)$ may be treated as a constant and the RSDH predictions of the scaling laws are not significantly altered.

III. EXPERIMENTAL DATA

Measurements of u in the first meter above ground were sampled at the Surface Layer Turbulence and Environmental Science Test (SLTEST) facility in the western deserts of Utah, USA, as part of the Idealized horizontal Planar Array study for Quantifying Surface heterogeneity (IPAQS) [38]. The SLTEST site is known for its low surface roughness, relatively predictable diurnal wind patterns in the early summer, and long unobstructed stretches of land in the dominant wind directions. Once the floor of Lake Bonneville, the surface of the SLTEST site naturally renews almost every year when the high water table recedes in late spring, leaving behind a stable crust that is smooth and essentially dust free with an aerodynamic roughness that ranges from sub-millimeter to less than ≈ 5 mm [39, 40]. These unique characteristics make the SLTEST site particularly suitable for probing high Re turbulent boundary layers with near-idealized boundary conditions.

The data were collected with nano-scale thermal anemometry probes (NSTAPs) operated in constant-current anemometry mode and sampled at 100 Hz. The sensing element of the NSTAP is a platinum wire filament 100 nm in thickness, 2 μm in width and 60 μm in length [41–43], providing high spatial resolution that ensures minimal spatial filtering effects. Five NSTAPs were deployed on an approximately logarithmic scale at heights $z = 0.0625$, 0.125, 0.25, 0.5, and 1.0 m above the ground during a three-day intensive sampling period (18 - 20 June 2018). A triaxial sonic anemometer (Campbell Scientific CSAT3) along with an adjacent fine-wire K-type thermocouple sampling at 20 Hz was stationed approximately 10 m west of the measurement tower at a height of 2 m. The tower and probe setup are shown in Fig. 2 and more details can be found elsewhere [44, 45].

Overall, 92 30-min records were collected, 15 of which occurred when the incoming wind aligned with the sensor direction, as verified by the sonic anemometer. Trends associated with a varying freestream velocity were then subtracted from the raw fluctuating signal following the methodology of Hutchins et al. [46], and the signal was high-passed at a frequency of 300^{-1} Hz. Stationarity of the mean longitudinal velocity $\overline{u}$ and the turbulence intensity $u'/\overline{u}$ at each measurement height were then assessed by using the reverse arrangement test and the runs test with a 95% confidence interval [47]. Non-stationary effects were observed in 5 records, which are subsequently discarded.

For each 30-min record, calibration of the sensors was achieved via collocated Pitot tubes that provided in-situ mean values. Simultaneous temperature measurements were also taken with adjacent T-NSTAP's (the temperature version of the NSTAP) calibrated with collocated E-type fine-wire thermocouples. An instantaneous application of

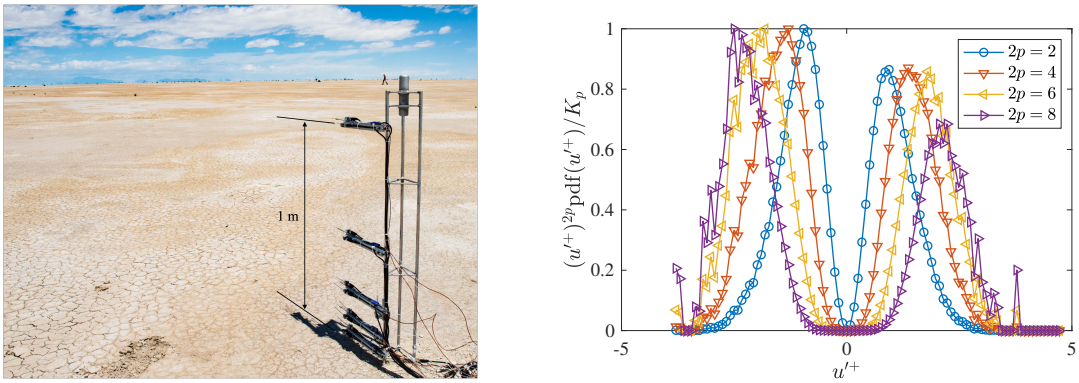

FIG. 2. Image of the 1-m measurement tower at the SLTEST site, which is known for its canonical nature due to unobstructed fetches of land with low surface roughness (left). Premultiplied pdf of normalized velocity fluctuations for data sampled at $z = 1$ m under near-neutral conditions for moments of order $2p = 2, 4, 6, 8$ (right). Each moment is normalized by K_p such that the maximum value is unity for clarity. Note the decay of the tail is sufficiently fast so that the estimation of the higher order pdf's is reasonably captured with the measurements.

the temperature compensation scheme proposed by Hultmark and Smits [48] was then implemented to account for the effects of changing ambient temperature. More details regarding the calibration procedure can be found in Huang et al. [44].

Lastly, the error due to limited statistical convergence of high-order moments $\overline{(u'^{2p})^+}^{1/p}$ is diagnosed. Due to unusually high estimated statistical convergence error, one more 30-min record was removed. As a representative case, the data sampled at $z = 1$ m ($z^+ \approx 1.7 \times 10^4$) is considered, and the errors calculated for each moment under each stability regime is featured in Table I. Given the estimated statistical convergence errors, the highest moment considered in the following analysis will be $2p = 8$. Following the approach described in Meneveau and Marusic [20], the premultiplied probability density functions (pdf) for $2p = 2, 4, 6, 8$ at $z = 1$ m under near-neutral conditions are shown in Fig. 2 (right). The amount of data reasonably captures the moment (commensurate with the area under the curve) up to $2p = 8$ in the sense that the decay of the tails is sufficiently fast.

The atmospheric stability condition of each record was assessed with two parameters: the Monin-Obukhov stability parameter $\zeta = z/L$ and the flux Richardson number R_f. The Obukhov length L is defined as

$$L = -\frac{u_*^3}{\kappa \left(g/\overline{\theta_v}\right) \overline{w'\theta_v'}}, \tag{24}$$

where $u_* = \sqrt{-\overline{w'u'}}$, g is the acceleration due to gravity, w', u' and θ_v' are the wall-normal velocity, streamwise velocity, and virtual potential temperature fluctuations, respectively, and $\overline{\theta_v}$ is the mean virtual potential temperature. The records were classified as unstable when $\zeta < -0.1$, near-neutral when $|\zeta| \leq 0.1$, and stable when $\zeta > 0.1$. Note that the magnitude of ζ values are small due to proximity to the boundary (that is, ζ values are small since $\zeta = z/L$ and $z < 1$ m). The flux Richardson number R_f is defined as

$$R_f = \frac{(g/\overline{\theta_v})\overline{w'\theta_v'}}{\overline{w'u'}(d\overline{U}/dz)}, \tag{25}$$

and is typically negative for unstable conditions, near-zero for neutral flows, and positive for stable flows. The two stability stability representations are related by $R_f = \zeta/\phi_M(\zeta)$, where ϕ_M is the stability correction function for momentum [49, 50].

The resulting 9 records under study are summarized in Table II with mean flow parameters and stability classifications calculated relative to the sonic anemometer. The $\mathcal{P}$ was estimated assuming a steady state and horizontally homogeneous conditions and choosing a coordinate system aligned with the mean wind as $\mathcal{P} = -\overline{u'w'}\frac{\partial \overline{u}}{\partial z}$. The $\overline{\epsilon}$ was separately estimated as

$$\overline{\epsilon} = \frac{1}{C_3(Re_\lambda)} \frac{\overline{\Delta u^3}}{r} \tag{26}$$

with the Re-dependent empirical constant $C_3 = -0.8 + 8.45 Re_\lambda^{-2/3}$, where $Re_\lambda = \sqrt{\overline{u'^2}}\lambda/\nu$ and $\lambda = \sqrt{15\nu\overline{u'^2}/\overline{\epsilon}}$ is

		$2p$				
		2	4	6	8	10
unstable	%	9	10	12	16	22
near-neutral	%	9	11	16	25	41
stable	%	7	10	18	31	48

TABLE I. Statistical convergence error estimates (%) for $\overline{(u'^{2p})^+}^{1/p}$ sampled at $z = 1$ m.

Date	LT	$\overline{u}$ (ms^{-1})	δ (m)	u_* (ms^{-1})	$\overline{w'\theta'_v}$ (Kms^{-1})	σ_u^+	σ_v^+	σ_w^+	$\sigma_u/\overline{u}$	$\mathcal{P}/\bar{\epsilon}$	ζ	R_f	Stability
21/06/2018	2000	7.55	60	0.28	-0.017	2.93	2.00	1.20	0.11	0.72	0.025	0.014	near-neutral
	2030	6.56	60	0.22	-0.018	3.97	3.26	1.38	0.13	1.21	0.053	0.040	near-neutral
	2200	6.60	60	0.24	-0.024	3.14	1.83	1.24	0.11	2.40	0.056	0.035	near-neutral
	2230	7.34	60	0.29	-0.029	3.63	2.07	1.19	0.14	1.26	0.038	0.016	near-neutral
22/06/2018	0400	2.85	30	0.094	-0.0056	5.16	5.23	1.44	0.17	0.79	0.19	0.19	stable
	0430	4.00	30	0.13	-0.0076	3.92	2.62	1.41	0.12	0.63	0.12	0.073	stable
	0500	3.14	30	0.11	-0.0066	2.82	3.69	1.25	0.10	1.14	0.146	0.077	stable
	0800	4.10	350	0.18	0.024	2.71	2.33	1.10	0.12	0.22	-0.13	-0.18	unstable
	0830	3.86	350	0.18	0.041	3.13	4.81	1.12	0.15	0.31	-0.13	-0.23	unstable

TABLE II. Mean flow properties and stability classifications relative to the sonic anemometer positioned at $z = 2$ m for the 30-min periods analyzed (local time LT = UTC + 6 h). The boundary layer height δ was estimated as discussed in the text, and R_f was estimated using both the sonic anemometer data and the mean velocity profile given by the NSTAPs evaluated at $z = 2$ m.

the Taylor microscale and iterated against Eq. 26. The mean velocity profile used in calculating $\mathcal{P}$ and R_f was given by the NSTAP measurements and evaluated at $z = 2$ m.

The boundary layer height δ was not directly measured and estimated based on the thermal stratification. Under near-neutral to slightly stable conditions, a $\delta \approx 60$ m was determined from comparing measured $\overline{u'^2}$ profiles to similarity formulations proposed by Marusic and Kunkel [17] as discussed in Huang et al. [44]. Under stable conditions, a $\delta \approx 30$ m was estimated from the formulation $\delta^2 \approx \sqrt{3}\kappa R_f\,(u_* L/|f_c|)$, where $f_c = 2\Omega\sin(\phi) \approx 1 \times 10^{-4}$ s^{-1} is the Coriolis parameter, Ω is the angular velocity of Earth's revolution, and ϕ is the site latitude [51]. For early morning hours but mildly unstable conditions, $\delta \approx 350$ m was estimated from the formulation $\delta = 0.2u_* f_c^{-1}$ [52]. Although this formulation was derived for slightly stable to near-neutral conditions, this approximation is plausible given that the unstable cases examined here are close to neutral stability and are sampled in early morning hours.

The pdf(u'/σ_u) for each sampled height and stability condition are presented in Fig. 3, where σ_u^2 is the velocity variance. Values of skewness $S_u = \overline{u'^3}/\sigma_u^3$ and kurtosis $K_u = \overline{u'^4}/\sigma_u^4$ are also included in the figure. It can be seen that the bulk of the statistics do not deviate appreciably from Gaussian, but the near-neutral and stable data sets exhibit slight super-Gaussian behavior. This super-Gaussian behavior has been observed in a number of wind tunnel experiments, but is in contrast to many DNS studies that indicate sub-Gaussian behavior in the inertial subrange [20, 53–55]. This could be explained by recent evidence that suggests the extent of the buffer layer may depend on the Reynolds number $\delta^+ = \delta u_*/\nu$ and extend to $z^+ \approx 3(\delta^+)^{1/2}$ in smooth-wall conditions [3, 56]. Under near-neutral conditions, this places the lowest two measurement heights within the buffer region where sweeps tend to dominate [54], explaining the increased S_u and K_u observed.

Nonetheless, with the onset of the logarithmic layer taken to be $z^+ = zu_*/\nu > 100$ [57], the lowest sampling height of $z^+ \approx 850$ may be well within the logarithmic region. The equivalent sand grain roughness was estimated to be $\approx$ 2.5 mm with the relation for a zero-pressure-gradient neutral boundary layer [44], so that the lowest sampling height is about 25 times that of the roughness height. The mean velocity and variance profiles are shown to exhibit logarithmic behavior in the region $10^3 < z^+ < 10^4$ as shown in Fig. 4.

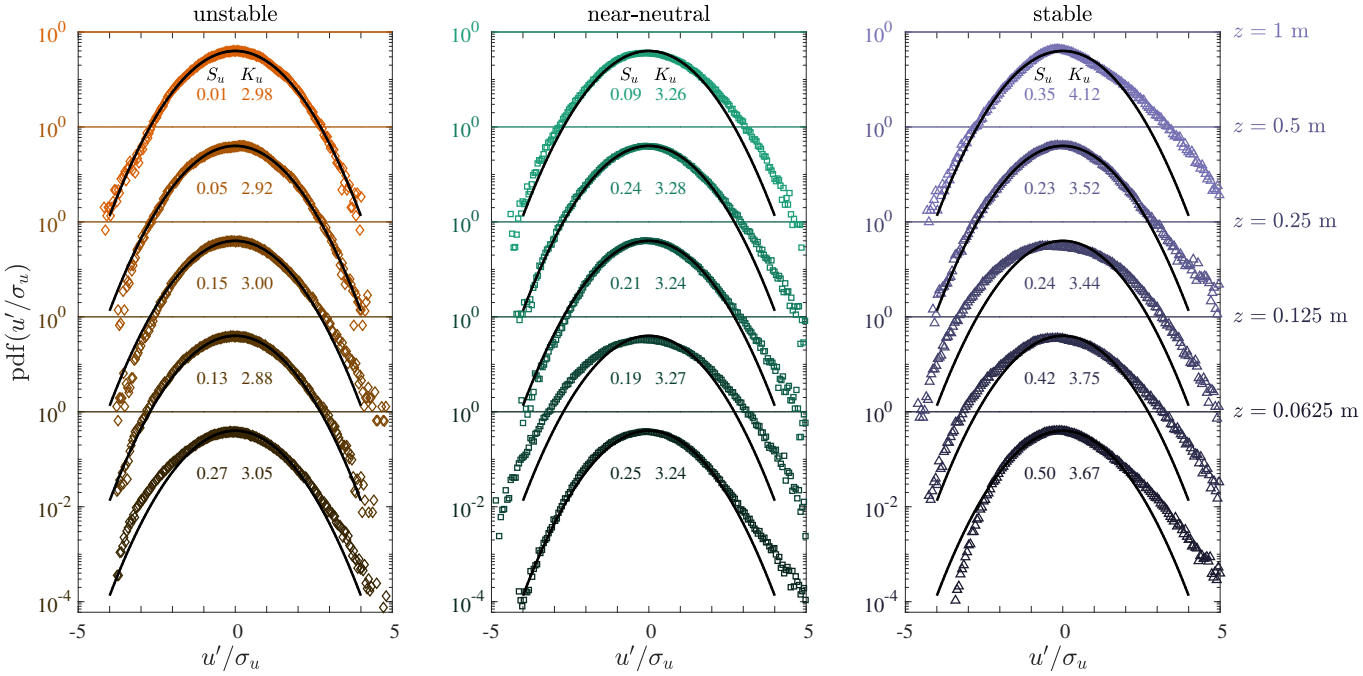

FIG. 3. Measured probability density functions (open circles) for the unstable (left), near-neutral (middle), and stable (right) stability conditions, ensemble-averaged across each 30-min period as listed in Table II and offset by an arbitrary amount to allow examination of each sampling height. For reference, a zero-mean and unit variance Gaussian distribution is included (thick-solid line), and skewness $S_{u'}$ and kurtosis $K_{u'}$ are also calculated at each height.

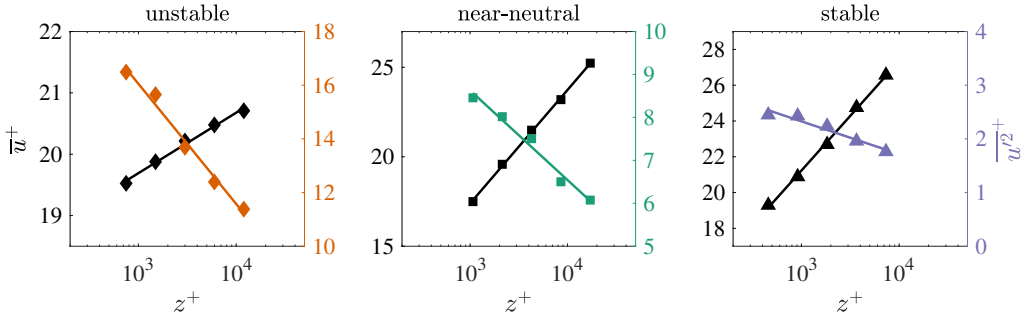

FIG. 4. The normalized mean velocity (left axis) and variance (right axis) profiles for unstable, near-neutral, and stable thermal stratification, averaged across all available 30-min periods for each stability regime.

IV. RESULTS

A. High-order Moments

The normalized measured first order spectra for each stability regime are presented in Fig. 5, where the normalization is based on u_* and z. These spectra show a -1 and $-5/3$ scaling separated at $k \approx 1/(\beta z)$ so that Eq. 12 applies directly. It can be seen that the effects of thermal stratification are manifested in a shift of the break point between the -1 and $-5/3$ scaling regions, which is also encoded in C_1 due to continuity at $k \approx 1/(\beta z)$ as discussed in Section II. Under near-neutral conditions, the break point occurs at $k \approx 1/z$ as expected. By inspection, for the spectra obtained under unstable conditions, the separation is shifted towards scales larger than z at $k \approx 1/(2.5z)$, and for those under stable conditions, the separation is shifted towards scales smaller than z at $k \approx 1/(0.125z)$. The model spectra (as in Fig. 1) is superposed onto the measured spectra with $\beta = 2.5, 1, 0.125$ for the unstable, near-neutral and stable conditions, respectively.

To examine the validity of Eq. 7, the measured high-order spectra $E_u^{(p)}(k)$ at $z = 1$ m and $z = 0.0625$ m are plotted against those predicted by the RSDH for $p = 2, 3, 4$ in Fig. 6 as an example. Similar trends are observed at all other

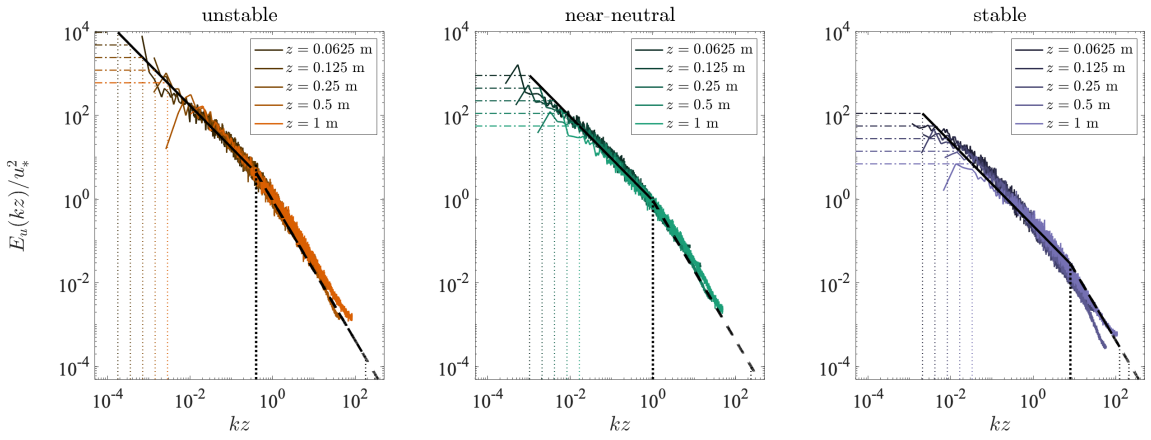

FIG. 5. Normalized spectra of the longitudinal velocity $E_u(kz)/u_*^2$ for the unstable (left), near-neutral (middle), and stable (right) thermal stratification as a function of normalized wavenumber kz. For each thermal stratification, there is a clear separation between the -1 (——) and the $-5/3$ (– –) scaling regimes as indicated by the black vertical dotted line (···) at $k \sim 1/(\beta z)$, with $\beta \approx 2.5, 1, 0.125$ from left (unstable) to right (stable) respectively. The $k = 1/\delta$ cutoff between the 0 (– · –) and the -1 scaling regimes are also shown for each measurement height and denoted by their respective colors.

heights and are not presented. In all cases and order p, the energy at the large scales are overestimated by the RSDH prediction, consistent with the observation that assumptions of the RSDH are less valid for the large scales. Under unstable and near-neutral conditions, it can be seen that the model is able to predict the high-order spectra well in the high wavenumber range (generally $kz > 1$). Notably, under mildly stable stratification as p increases, the RSDH prediction underestimates the measured spectra in the high wavenumbers and compensates for the overestimation in the low-wavenumber region.

Measured $(\overline{u'^{2p}}^+)^{1/p}$ are shown in Fig. 7 for $2p = 2$, 4, 6, 8 and are consistent with a generalized log law in the inertial region, i.e. where the variance ($p = 1$ case) displays a logarithmic scaling. For $p > 1$, predicted $(\overline{u'^{2p}}^+)^{1/p}$ was estimated via Eq. 17 and plotted with dashed lines.

Overall, acceptable agreement can be seen between the modeled and measured A_p for all thermal stratification, which are plotted in Fig. 8 (left). The prediction for A_p as explained by random sweeping under near-neutral conditions falls close to the prediction $A_p = A_1 \left[(2p-1)!!\right]^{1/p}$ based on Gaussian statistics proposed by Meneveau and Marusic [20], which is represented by the solid gray line. In contrast to the sub-Gaussian behavior seen in Meneveau and Marusic [20], the measured A_p values here exhibit slightly super-Gaussian behavior, although this curvature may be attributed to experimental uncertainty.

The predicted B_p values appear to be less robust, with the agreement to measured data dependent on stability as shown in Fig. 8 (right). The modeled B_p values capture the measured data well under stable conditions, but overestimates the measured B_p under near-neutral and especially under unstable stratification, reflective of the observations in Fig. 6. This may also be a result of the high sensitivity of B_p values to the value of A_p. In the following section, the validity of the RSDH under various thermal stratification will be explored.

B. Evaluation of The Random Sweeping Decorrelation Hypothesis

The assumptions inherent to the RSDH are now explored under varying thermal stability to test its validity. Formulating the RSDH in physical space facilitates an assessment of the independence between u'^k and Δu^l with varying r. As an example, Eq. 19 for $m = 2$ is given by

$$D_u^2(r) = 4\,\overline{u'^2 \Delta u^2} + 12\overline{u'^1 \Delta u^3} + \ldots. \tag{27}$$

The correlation coefficient $\rho_{\Delta u^2, u'^2}(r)$ determined by correlating the series u'^2 with the series Δu^2, and the coefficient $\rho_{\Delta u^3, u'}(r)$ determined by correlating the series u' with the series Δu^3 can then be determined as a function of r/z to assess the statistical independence between u'^k and Δu^l for high-order moments. Recall that the RSDH assumes all of these correlations are negligible at all r. The coefficients $\rho_{\Delta u^2, u'^2}(r)$ and $\rho_{\Delta u^3, u'}(r)$ for the data series taken at $z = 1$ m under near-neutral conditions are explored in Fig. 9 as an example. The same trend is observed in all other sampled heights under all stability conditions and are not presented.

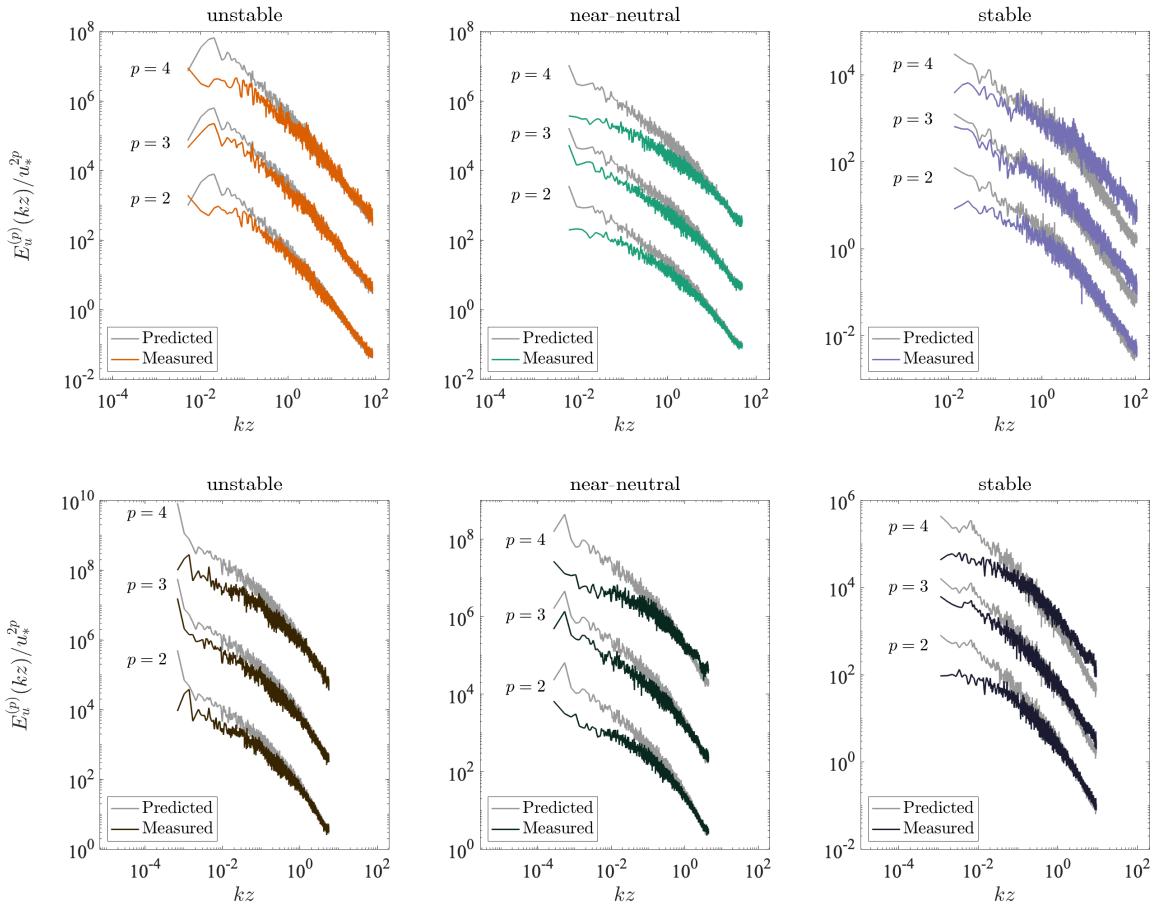

FIG. 6. Normalized high-order spectra of the longitudinal velocity $E_u^{(p)}(kz)/u_*^2$ for $p = 2, 3, 4$ under unstable (left), near-neutral (middle), and stable (right) thermal stratification as a function of normalized wavenumber kz at $z = 1$ m (top row) and at $z = 0.0625$ m (bottom row) . The colored records represent measured $E_u^{(p)}(k)$ and the gray records represent the corresponding prediction $\alpha(p)\overline{u'^2}^{p-1}E_u(k)$ (Eq. 7).

It is evident from Fig. 9 that the correlation coefficients remain significant at all scales, demonstrating a lack of statistical independence between velocity and velocity increments at high moments and a violation of the RSDH. However, it can be seen that the odd ($\rho_{\Delta u^3,u'}(r)$) and even ($\rho_{\Delta u^2,u'^2}(r)$) ordered coefficients are opposite in sign and similar in value. This suggests some compensatory mechanisms exist such that even though the underlying assumptions are not valid, the RSDH may be operationally functional, thus explaining its partial success in predicting the high-order moments as discussed in the previous section.

To further investigate the scale-wise applicability of the RSDH, Fig. 10 presents $d^m(r)$ and $g^m(r)$ for the longitudinal velocity measured under unstable, near-neutral, and stable thermal stratification measured at $z = 1$ m as a representative case. Similar trends for $d^m(r)$ and $g^m(r)$ are observed at other heights and are included in Appendix A for completeness. Overall, the scale dependence of $d^m(r)$ and $g^m(r)$ means that the RSDH is not impacting all the scales equally and may not be valid across all scales (as discussed, $d^m(r) = 1$ and $g^m(r) = 1$ if the RSDH holds), and these distortions seem to be more evident as the moment increases.

At small scales (as $r/z \to 0$), $g^m(r)$ appears to approach a value of 1 as predicted by the RSDH for all stability conditions. For $d^m(r)$, the unstable condition shows an approach to 1 as r decreases, while the $d^m(r) > 1$ seen in the near-neutral and stable cases is a signature of intermittency corrections.

On the other end, both $d^m(r)$ and $g^m(r)$ tend toward a constant and exhibit weaker scale dependency at large scales (as $r/z \to \infty$). This suggests that even though the RSDH is not entirely correct for the large scales, $\Omega(\cdot)$ may be treated as a constant past a certain separation and the scaling laws predicted by the RSDH for $D_u^m(r)$ from $D_u(r)$ (or equivalently $E_u^p(k)$ from $E_u(k)$) are not altered significantly. Generally, it can be seen that $d^m(r)$ approaches a value closer to 1 under stable conditions at all heights compared to the unstable or near-neutral stratification (for data at $z = 1$ m, $d^m(r \to \infty) \approx 0.4$ under unstable conditions, $d^m(r \to \infty) \approx 0.5$ under near-neutral conditions, and

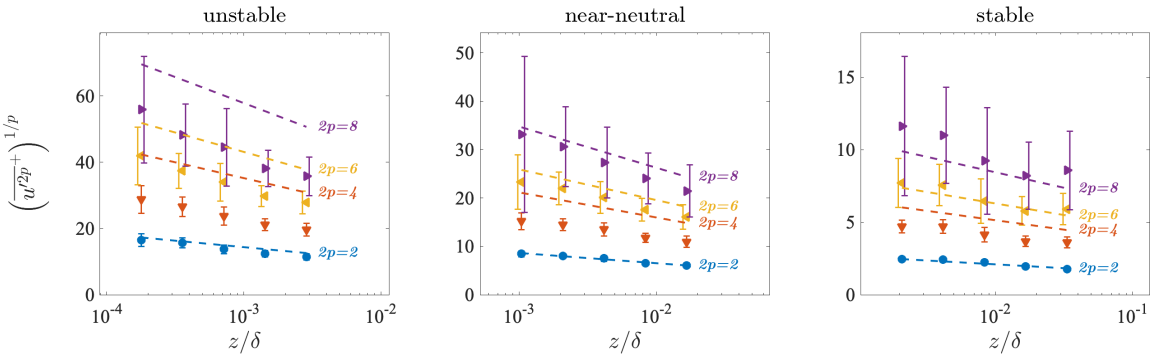

FIG. 7. High-order moments of the longitudinal velocity under unstable (left), near-neutral (middle), and stable (right) conditions for $2p = 2, 4, 6, 8$, averaged across available datasets for each thermal stratification. The dashed lines represent the high-order moments as predicted by Eq. 17.

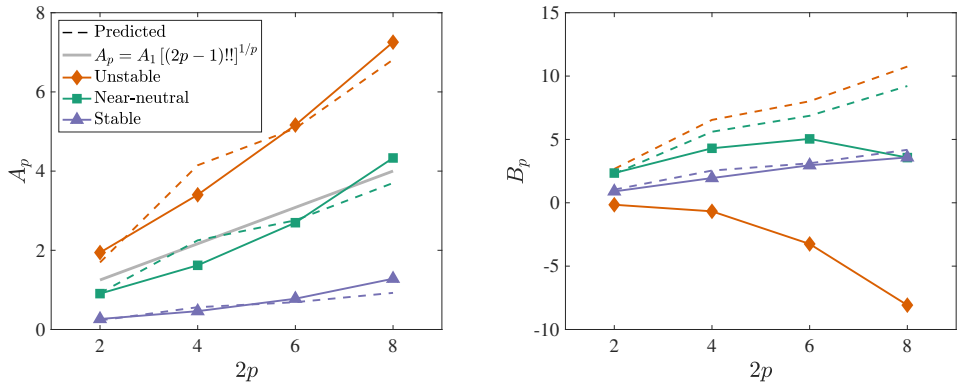

FIG. 8. Coefficients A_p (left) and B_p (right) as a function of moment order $2p$ across the 3 stability regimes. The dashed lines represent the coefficients as predicted by Eq. 17, and the gray line represents the coefficients as predicted by $A_p = A_1\,[(2p-1)!!]^{1/p}$.

$d^m(r \to \infty) \approx 0.8$ under stable conditions). This suggests that the RSDH over-predicts the data under unstable or near-neutral stratification more so than it does under stable stratification, which could explain the variations in B_p observed in Fig. 8.

Here, the separation at which this scale independence occurs, r_o, was determined by first smoothing $d^m(r)$ and $g^m(r)$ using a binning method, and then calculating for r when $|\mathrm{d}(d^m(r))/\mathrm{d}(r/z)| < 0.001$ for all moment orders considered (not shown). Under this somewhat arbitrary threshold, the resulting r_o values for each height and stability condition are presented in Fig. 11. Overall, r_o values for $d^m(r)$ and $g^m(r)$ are comparable, and it can be seen that r_o appears well-collapsed with distance-from-the-wall scaling with no discernible sensitivity to the stability condition. The scale independence occurs at $r_o/z \approx 60$, which is higher than the $r_o/z \approx 5$ value reported in Katul et al. [21] for $d^m(r)$. While the exact values of r_o are sensitive to the threshold chosen to calculate it (i.e. setting $|\mathrm{d}(d^m(r))/\mathrm{d}(r/z)| < 0.01$

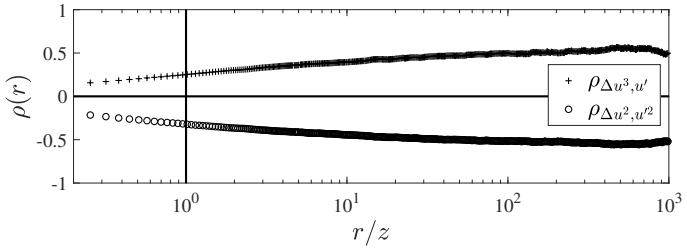

FIG. 9. Variations of $\rho_{\Delta u^2,u'^2}(r)$ and $\rho_{\Delta u^3,u'}(r)$ for $z = 1$ m under near-neutral stability. Data at all other sampling heights and thermal stratification show similar trends. The RSDH assumes $\rho(r)$=0.

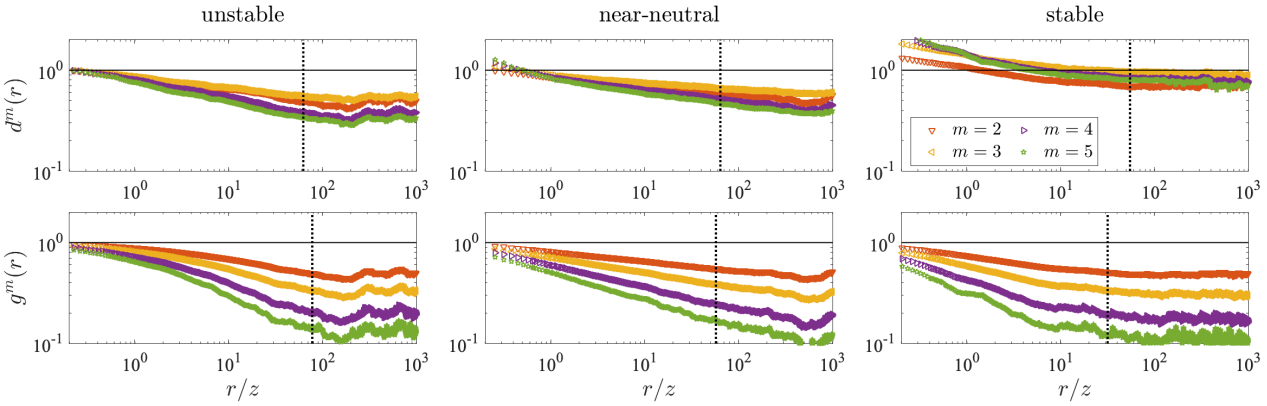

FIG. 10. Variations of $d^m(r)$ (top row) and $g^m(r)$ (bottom row) with r/z for $m = 2, 3, 4, 5$ for data collected at $z = 1$ m under unstable (left column), near-neutral (middle column), and stable (right column) conditions. The RSDH requires $d^m(r) = 1$ and $g^m(r) = 1$ (solid horizontal lines). The r_o/z value at which $d^m(r)$ and $g^m(r)$ become approximately constant insensitive to increasing r is marked with a vertical dotted line.

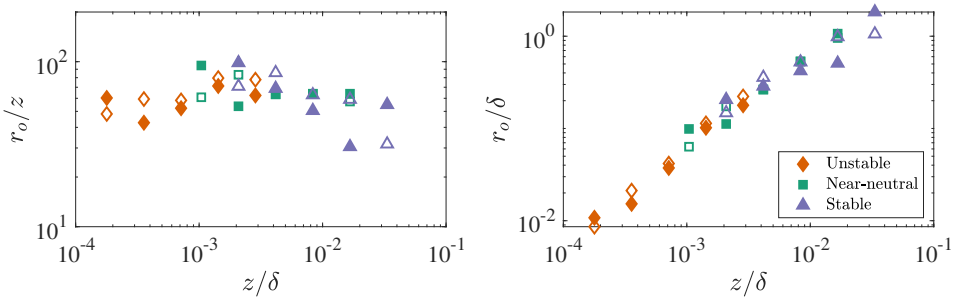

FIG. 11. The separation r_o at which scale independence of $d^m(r)$ (solid symbols) and $g^m(r)$ (open symbols) occur, normalized with distance from the wall (left) and with outer flow scaling (right). The variations of r_o/δ (right) are presented only for completeness to illustrate outer-layer size effects for r_o.

instead of 0.001 results in $r_o/z \approx 10$), its collapse in wall scaling despite of thermal stratification is a persistent feature.

By contrast, the RSDH seems to exhibit the most distorted effects in the intermediate scales. To illustrate, Fig. 12 (left column) shows $D_u^m(r)$ and $m^2\overline{u'^{2m-2}}\ \overline{\Delta u^2}$ against r/z bounded by $z < r < r_o$ for $m = 2, 3, 4, 5$ under near-neutral thermal stratification measured at $z = 1$ m. To investigate and capture this non-constant deviation in $\Omega(\cdot)$ from unity, a regression problem can be formulated following Katul et al. [21] with measured $D_u^m(r)$ against measured $m^2\overline{u'^{2m-2}}\ \overline{\Delta u^2}$. A regression slope A_m with increasing m can then be determined, as demonstrated in Fig. 12 (right column). The presented data are again bounded by $z < r < r_o$, and the RSDH prediction of $A_m = 1$ is also plotted (dashed lines). It can be seen that while sub-unity A_m is found for all m, $D_u^m(r)$ is still correlated linearly with $m^2\overline{u'^{2m-2}}\ \overline{\Delta u^2}$ at all m.

When raising A_m to a power of $1/m$, as shown in Fig. 13, $A_m^{1/m} \approx 0.72 \pm 0.17$ under unstable conditions, $A_m^{1/m} \approx 0.71 \pm 0.17$ under near-neutral conditions, and $A_m^{1/m} \approx 0.68 \pm 0.18$ under stable conditions (or collectively, $A_m^{1/m} \approx 0.7 \pm 0.2$), implying that $\Omega(\cdot)$ from this intermediate region may be captured by a constant insensitive to m. Katul et al. [21] also reported a similar value and trend ($A_m^{1/m} \approx 0.72 \pm 0.05$) under near-neutral conditions for data collected over an ice sheet, which suggests that deviation from the RSDH in the $z < r < r_o$ region could be captured and accounted for through a quasi-constant $A_m^{1/m}$. Note that the moment order $2m = 10$ is included in this analysis and shows a value of $A_m^{1/m}$ consistent with those of lower orders despite higher estimated statistical convergence errors, indicating that $A_m^{1/m}$ could be less sensitive to such errors.

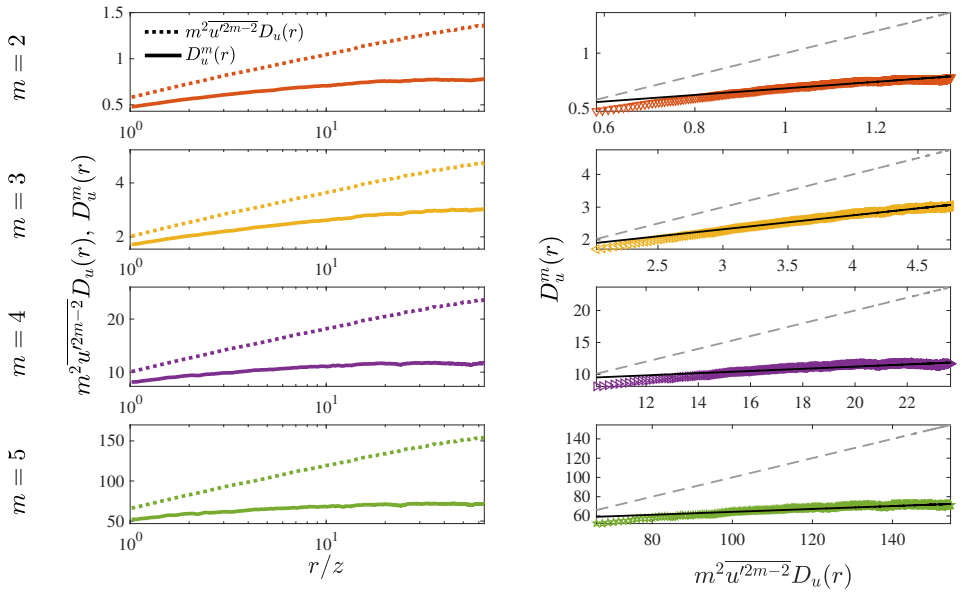

FIG. 12. Left column: measured $D_u^m(r)$ (——) and $m^2\overline{u'^{2m-2}}D_u(r)$ (- - -) against r/z for $m = 2, 3, 4, 5$ bounded by $z < r < r_o$ under near-neutral stability conditions at $z = 1$ m. Right column: Variations of measured $D_u^m(r)$ against $m^2\overline{u'^{2m-2}}D_u(r)$ for $m = 2, 3, 4, 5$ bounded by $z < r < r_o$ under near-neutral stability conditions at $z = 1$ m. The dashed lines represent a slope of 1 as predicted by the RSDH. The solid black lines are linear fits to the data to calculate A_m.

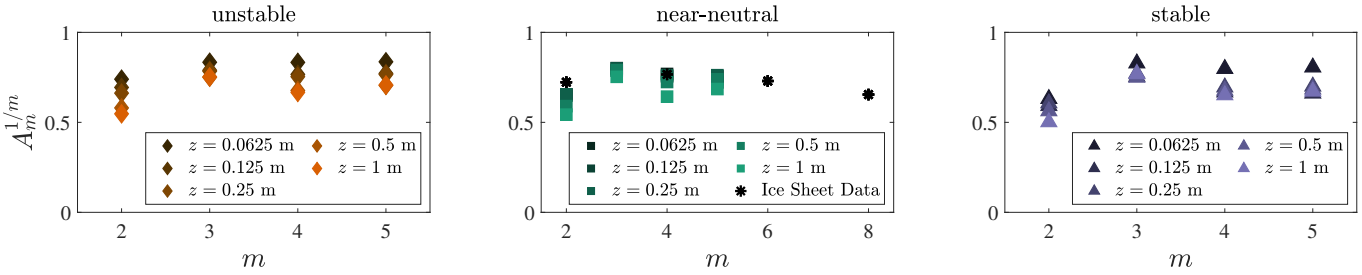

FIG. 13. The regression slopes $A_m^{1/m}$ against m at all heights under unstable (left), near-neutral (center) and stable (right) conditions.

V. STUDY LIMITATIONS AND DISCUSSION

A model for the high-order moments of the turbulent longitudinal velocity was proposed and its coefficients A_p and B_p evaluated using new experiments. These experiments were conducted in the atmospheric surface layer near the ground at small $z/\delta \leq 0.01$, very high Reynolds number, and mild thermal stratification ($|\zeta| \leq 0.2$). A near-log behaviour with z^+ for $\overline{u}^+$ and $\overline{u'^2}^+$ were confirmed for the experimental conditions considered. Using standard constants in turbulence, the predicted A_p was reasonably reproduced by the experiments while the predicted B_p deviated from measurements except for slightly stable conditions where $\mathcal{P}/\bar{\epsilon}$ is closest to unity. An assessment of the assumptions and data limitations follow in an effort to offer a model validation. With regards to model assumptions, these include (i) the shape of the assumed longitudinal velocity spectrum, (ii) the Gaussian assumption for u', and (iii) the ability of the RSDH to predict high-order spectra from the longitudinal velocity spectrum.

While the model spectrum presented in Fig. 1 led to analytical tractability, it is an idealization that is likely to overestimate the energy content in the low wavenumber region beyond what the current data set is able to resolve. The model spectrum extends the k^{-1} scaling at low wavenumbers to $k\delta = 1$ and scales as a constant below $k\delta = 1$. In reality, one would expect the spectrum to decay to zero at $k \to 0$ (for large scales) and to scale at least as k^2 (e.g. in the Saffman spectrum). Thus, the integration of this model spectrum from $k = 0$ to $k = \infty$ may be amplifying the variance in the idealized shape, so that the corresponding A_1 and B_1 values may not be entirely compatible with measurements that do not resolve such very large eddies. For example, if the region below $k\delta = 1$ scales as k^2 in reality, the model spectrum would overestimate the energy in this region by three times, which in turn also overestimates B_1.

As seen in Fig. 5, these larger scales are not resolved by the sampled data as a trade-off exists in atmospheric flow studies between the length of the sampling period and stationarity. Another model idealization here is the extension of the inertial subrange to the Kolmogorov microscale after which an abrupt energy cutoff was introduced. For scales commensurate with $k\eta > 0.1$, the energy spectrum exhibits a number of features such as a bump due to a bottleneck in the energy cascade followed by an exponential cutoff (e.g. the Pao spectrum) as reviewed elsewhere [58]. Resolving these process becomes significant when $\beta z/\eta < 10$. However, for $\beta z/\eta > 100$, these processes become less significant because the interest is in the integrated spectrum. Thus, extending the inertial subrange to $k\eta = 1$ followed by a cutoff overestimates the energy content for $k\eta < 1$ but the cutoff $k\eta > 1$ underestimates the remaining fine-scaled energy content, so that the effect of such over-and-underestimation on the total energy content becomes minor. Nonetheless, the idealized spectrum provides a straightforward analytic result for the theory at hand, and its integrated value appears to reasonably match the measured variances for the current data sets (as seen in Fig. 7 for the $2p = 2$ cases).

The measured flow statistics are not Gaussian but do not appreciably deviate from Gaussian when evaluated using the flatness and skewness factors. The flatness factor across all experiments (and z^+) varied from 2.9-4.0, but the majority of the runs were close to 3.0. The skewness, however, was positive across all runs. The positive skewness may indicate that roughness sublayer effects have impacted the u' statistics consistent with numerous laboratory experiments [54]. This impingement appears to not have affected A_p though.

The RSDH was evaluated in spectral and physical space for high-order spectra and structure functions. The RSDH was derived under the assumption small eddies are experiencing sweeps due to the energy content of larger eddies. The cutoff scale defining large and small eddies remains unclear when extending this analysis for eddy sizes larger than inertial ($r/z > 1$). The work here suggests that in physical space and beyond eddy sizes dictated by r_o (with $10 < r_o/z < 100$), corrections to RSDH are scale independent. For eddy sizes ($r_o/z < 10$) where some scale dependency exists in the correction to RSDH, compensatory mechanisms also exist and suggest operational viability. Taylor's frozen turbulence hypothesis was employed here and its usage could cause scale distortions when converting time to domain scale. The overall turbulent intensity $\sigma_u/\overline{u} \leq 0.17$ for all 30-min periods. While this turbulent intensity is small, it is not ideal. Nonetheless, two measures ($d^m(r)$ and $g^m(r)$) were used to evaluate scale-wise interactions distorting predictions from RSDH. These two measures cannot be impacted identically by Taylor's hypothesis; yet, they both agree on the strength of the scale-wise interactions and the cutoff r_o/z.

A distinction between field and laboratory flows is that unlike in controlled settings where the wind direction aligns precisely with the x-axis, there are no restrictions from the wind direction in the atmosphere so that the separation between the u and v components is less clear. Any misalignment between the x-axis and the incoming wind could then result in biases from the v-component that reduces the effective production measured. This could explain why C_1 determined from fitting $E_u(k) = C_1 u_*^2 k^{-1}$ to the first order spectrum in atmospheric studies ($C_1 = 0.95 - 1.1$) tends to be lower than A_1 determined from $\overline{u'^2}$ profiles obtained in laboratory conditions ($A_1 = 1 - 1.27$). As an overview, reported A_1 and C_1 values from sample laboratory and field studies are summarized in Table III. Recall that under the proposed theory, $A_1 = C_1$ (Eq. 13). Values of A_1 and C_1 from the current study are also included; it can be seen that A_1 from the measured data is close to the model spectrum value of $C_1 = C_o\kappa^{-2/3} \approx 0.92$ with $\kappa = 0.4$, while C_1 from measured spectra is slightly higher at 1.01 (though as mentioned, the measured spectra do not fully resolve the scales in the -1 region).

Two other issues stand out in terms of experimental limitations: the first is that variable δ across runs was not measured and was only estimated from near-surface heat and momentum fluxes. The second is that the estimated ratio $\mathcal{P}/\overline{\epsilon}$ are approximately 0.27, 1.40, 0.85 for the unstable, near-neutral, and stable stratification, respectively, when averaged across the available 30-min periods. Hence, The $\mathcal{P}/\overline{\epsilon} = 1$ assumption of the logarithmic layer is reasonably valid only under weakly stable conditions. As mentioned, the thickness of the roughness sublayer could have also impinged on the log layer, affecting such assumptions in the log region. Perhaps the results here remain insensitive to $\mathcal{P}/\overline{\epsilon} = 1$ because the high-order spectra scale with $(\overline{\epsilon})^{2/3}$, a sub-unity exponent.

It will be remiss if errors associated with the measured u_* value (obtained from a nearby but not collocated sonic anemometer) and the assumption of a constant flux layer are not flagged. These errors could also lead to inaccuracies in the calculated values of A_1 and B_1. Sonic anemometers have an averaging path length of 0.1m and can filter out a non-negligible portion of the momentum and heat flux co-spectra (especially at such a low $z = 2$ m). This underestimation can lead to an underestimation in u_* values used in the normalization here.

Despite the aforementioned theoretical and experimental limitations, agreement was found between predicted and measured $\overline{u'^{2p}}^+$ for all thermal stratification examined up to $2p = 8$. Measured A_p were reasonably captured by the model while measured B_p showed the most deviation under unstable and near-neutral conditions, a result that was not considered in a prior study [21]. Investigation into the assumptions of the RSDH in physical space suggests that it may not be entirely correct, but viewed as operationally viable due to inherent compensatory effects. Further, the deviations from the RSDH predictions appear to be characterized by two regions that seem insensitive to the thermal stratification examined here: one at large separations, where the RSDH appears to be plausible but with a constant offset, and one at the intermediate scales bounded by $1 < r/z \lesssim 60$ where the distortions seem to be well-captured

	δ^+	Authors	Flow Type
A_1			
$1.19 - 1.27$	$0.28 - 1.9 \times 10^4$	Meneveau and Marusic (2013) [20]	Boundary layer in wind tunnel (Melbourne HRNBLWT)
1.25	9.8×10^4	Hultmark (2012) [7]	Pipe flow (Princeton Superpipe)
1.21	6.9×10^4	Marusic et al. (2013) [3]	Channel flow (William B. Morgan LCC)
0.91	1.0×10^6	current study	ASL flow (SLTEST)
C_1			
1	950	Katul and Chu (1998) [28]	Open channel over a smooth surface
1	1.9×10^4	Antonia and Raupach (1993) [59]	Inner region of a rough-wall laboratory boundary layer
0.95	–	Kader et al. (1989) [33]	ASL flow (Tsimlyansk Field Station)
1.1	–	Katul et al. (1995) [36]	ASL flow over dry lake bed (Owen's Lake)
1.01	–	Pond et al. (1966) [34]	ASL flow over the sea
1.01	1.0×10^6	current study	ASL flow (SLTEST)

TABLE III. Sample studies of reported A_1 (from fitting equation 2 to the $\overline{u'^2}^+$ profile) and C_1 (from fitting $E_u(k) = C_1 u_*^2 k^{-1}$ to first-order spectrum) values under neutral conditions. The Reynolds number δ^+ is included when available.

by the quasi-constant $A_m^{1/m} \approx 0.72 \pm 0.2$. This suggests possible avenues for correction in future modeling efforts of $\overline{u'^{2p}}^+$ that could account for the deviations in the underlying RSDH assumption.

VI. CONCLUSION

The logarithmic relation of $\overline{u'^{2p}}^+$ with z/δ as explained by the RSDH and the presence of a -1 power law scaling regime in $E_u(k)$ is examined with longitudinal velocity data collected within one metre above the salt flats of Utah at very high Reynolds number. Building upon Katul et al. [21], which examined the theory at a single sampling height under near-neutral conditions, the current study examines for the first time the validity of the proposed theory across the logarithmic layer with multi-level data, and additionally expands the theory to account for mild thermal stratification.

Due to the proximity of the measuring heights to the surface, $\zeta = z/L$ does not vary significantly from near-neutral stratification and spanned mildly unstable to mildly stable stability conditions ($-0.13 \leq \zeta \leq 0.19$). As a result, measured $E_u(k)$ are shown to be described by a two-regime idealized spectrum such that the effect of the varying stratification is not strong enough to introduce different coherent structures that would alter the -1 scaling regime. Nonetheless, the varying atmospheric stability conditions do impart a noticeable signature in the spectra as it is seen to shift the characteristic eddy size where the -1 and the $-5/3$ power laws intersect from $1/z$ to $1/(\beta z)$, where β is a constant. This shift allowed for an extension of the proposed theory to incorporate effects of mild thermal stratification through β, from which coefficients of the generalized logarithmic law can be determined via well-known coefficients C_o and κ. Based on only two assumptions – that the RSDH applies (turbulent eddies are non-interacting and remain undistorted) and that the statistics are Gaussian – the proposed theory has been shown to be able to predict higher order statistics from the first order spectrum. Compared to prior work that used Gaussian statistics, the topology of attached eddies in physical space, and the non-interacting eddies assumption to explain the logarithmic relation of $\overline{u'^{2p}}^+$ with z/δ (after a lengthy derivation), the work here offers additional foresight: (i) Deviations from logarithmic relation of $\overline{u'^{2p}}^+$ with z/δ can now be explicitly linked to the shape of the velocity spectrum (if known); (ii) the interactive effects of large- and small eddies can be traced to coefficients linking $\overline{u'^{2p}}^+$ with z/δ; (iii) all the coefficients derived here emerge from well-established constants in boundary layer theories; (iv) moving beyond attached and detached eddies, the effect of very large eddies ($k\delta < 1$) can be accommodated in the present framework if their spectral signatures are known.

It is worth noting that the proposed theory could apply to both smooth and rough wall conditions with the same coefficients. While the mean velocity profile is highly dependent on the roughness of the boundary, the velocity variance profile is less sensitive to the underlying surface roughness. That is, while the roughness of the wall plays an important role in momentum transport and results in an offset in the logarithmic u^+ profile (smooth walls tend to maintain the coherency of coherent structures for longer, while the presence of roughness elements tends to disturb these structures and randomize their impact), under the view that large scale eddies from the outer layer impinge at the wall, the spectrum (and velocity variance) is less sensitive to surface conditions. The results obtained by

interpreting the higher order spectra via the RSDH therefore should apply to both smooth and rough wall conditions.

Here, a model spectrum was adopted that allowed for a shift between the break point of the -1 and $-5/3$ scaling regions to account for mild thermal stratification. Although the cases examined are close to near-neutral stability, this is a necessary first step to understanding more complicated cases where the entire shape of the spectrum shifts and the model spectrum no longer applies. Future efforts can then be focused on developing models for the first order spectrum, from which the higher order statistics can be predicted. The current work also sets the stage to understanding interaction between the large and small scales and to what degree their interactions are important. Since the RSDH precludes interactions between large and small scales, it provides the reference calculation for results when there are no interactions. Building upon this work, the effect of interactions on bulk statistics like $\overline{u'^{2p}}^{+}$ can then be examined and compared to this reference case.

Lastly, whether the RSDH can also be used to predict the variation with z/δ of high-order statistics for scalars that are transported without inherent dynamic interactions in the flow has not been explored and is a topic for future investigations.

ACKNOWLEDGMENTS

The authors would like to thank C. Byers and especially M. Fu for their help in editing the paper. Katul acknowledges support from NSF-AGS-1644382, NSF-AGS-2028644 and NSF-IOS-1754893. Huang acknowledges support from the Department of Defense (DoD) through the National Defense Science and Engineering Graduate Fellowship (NDSEG) Program, NSF-AGS-1649049, and ONR grant N00014-21-1-2296 (Fatima Multidisciplinary University Research Initiative) administered by the Marine Meteorology and Space Program of the Office of Naval Research.

Appendix A

Variations of $d^m(r)$ and $g^m(r)$ with r/z for $m = 2, 3, 4, 5$ for data collected at all heights are presented for completeness.

[1] L. Prandtl, Bericht über untersuchungen zur ausgebildeten turbulenz, J. Appl. Math. Mech. **5**, 136 (1925).
[2] T. Von Kármán, Mechanische ähnlichkeit und turbulenz, Gött. Nachr. , 58 (1930).
[3] I. Marusic, J. P. Monty, M. Hultmark, and A. J. Smits, On the logarithmic region in wall turbulence, J. Fluid Mech. **716**, R3 (2013).
[4] A. J. Smits, B. J. McKeon, and I. Marusic, High-Reynolds number wall turbulence, Annu. Rev. Fluid Mech. **43** (2011).
[5] J. Jiménez, Cascades in wall-bounded turbulence, Annu. Rev. Fluid Mech. **44**, 27 (2012).
[6] A. Townsend, *The structure of turbulent shear flow* (Cambridge University Press, 1976).
[7] M. Hultmark, M. Vallikivi, S. C. C. Bailey, and A. Smits, Turbulent pipe flow at extreme Reynolds numbers, Phys. Rev. Lett. **108**, 094501 (2012).
[8] T. Banerjee and G. G. Katul, Logarithmic scaling in the longitudinal velocity variance explained by a spectral budget, Phys. Fluids **25**, 125106 (2013).
[9] A. Yaglom, Fluctuation spectra and variances in convective turbulent boundary layers: A reevaluation of old models, Phys. Fluids **6**, 962 (1994).
[10] T. Banerjee, G. G. Katul, S. T. Salesky, and M. Chamecki, Revisiting the formulations for the longitudinal velocity variance in the unstable atmospheric surface layer, Q. J. R. Meteorol. Soc. **141**, 1699 (2015).
[11] A. E. Perry and C. J. Abell, Asymptotic similarity of turbulence structures in smooth-and rough-walled pipes, J. Fluid Mech. **79**, 785 (1977).
[12] A. E. Perry, S. Henbest, and M. S. Chong, A theoretical and experimental study of wall turbulence, J. Fluid Mech. **165**, 163 (1986).
[13] A. E. Perry and J. D. Li, Experimental support for the attached-eddy hypothesis in zero-pressure-gradient turbulent boundary layers, J. Fluid Mech. **218**, 405 (1990).
[14] J. Jimenez and S. Hoyas, Turbulent fluctuations above the buffer layer of wall-bounded flows, J. Fluid Mech. **611**, 215 (2008).
[15] J. Kaminsky, J. Klewicki, and B. Birnir, Application of the stochastic closure theory to the townsend-perry constants, Phys. Rev. E **100**, 061101 (2019).
[16] R. Örlü, A. Segalini, J. Klewicki, and P. H. Alfredsson, High-order generalisation of the diagnostic scaling for turbulent boundary layers, J. Turbul. **17**, 664 (2016).

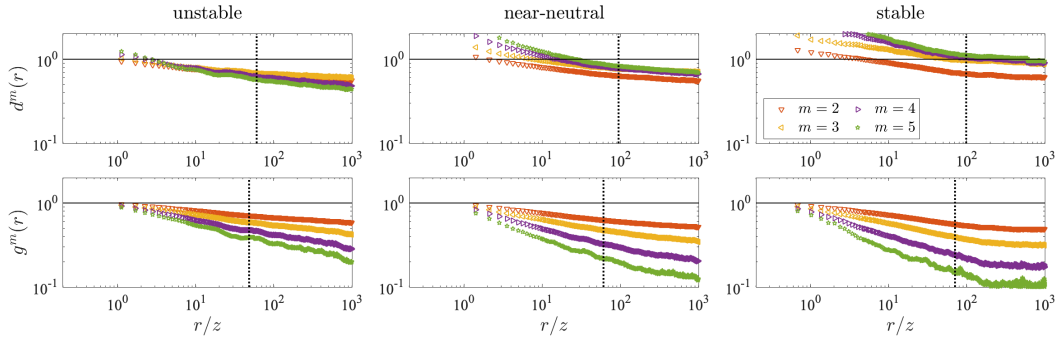

FIG. 14. Same as in Fig. 10 but for $z = 0.0625$ m.

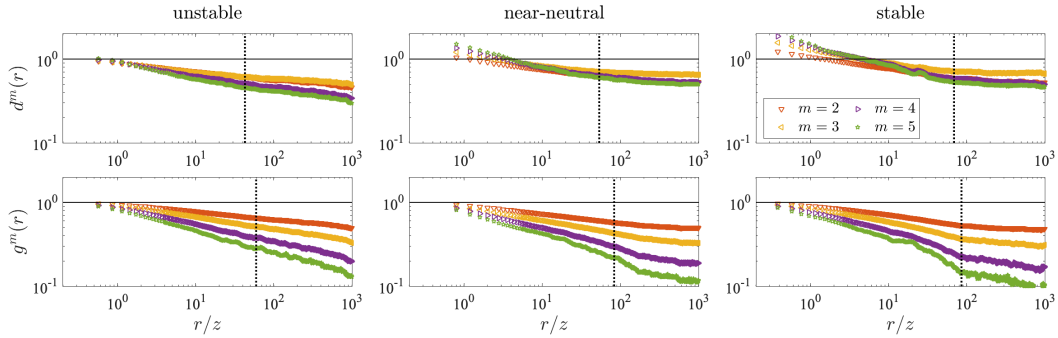

FIG. 15. Same as in Fig. 10 but for $z = 0.125$ m.

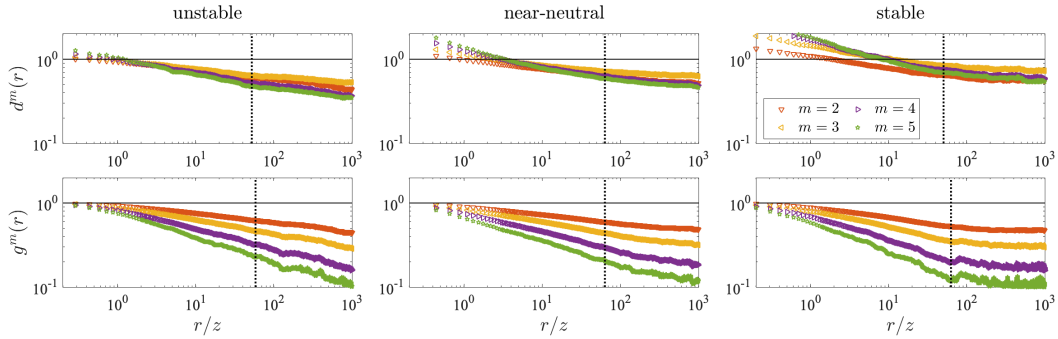

FIG. 16. Same as in Fig. 10 but for $z = 0.25$ m.

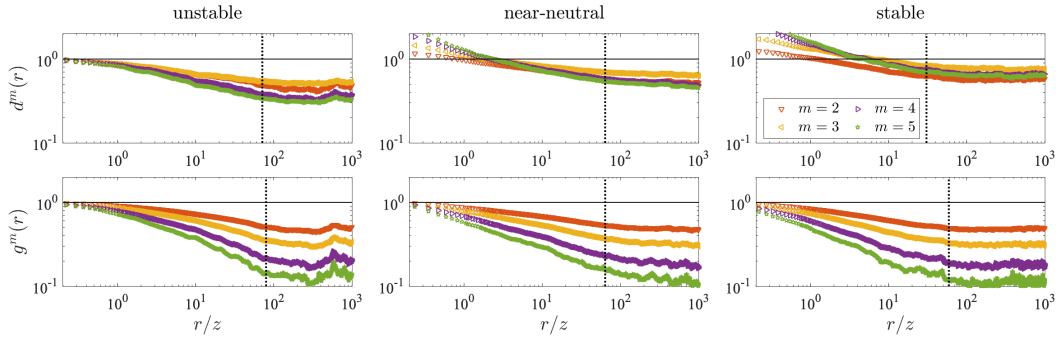

FIG. 17. Same as in Fig. 10 but for $z = 0.5$ m.

[17] I. Marusic and G. J. Kunkel, Streamwise turbulence intensity formulation for flat-plate boundary layers, Phys. Fluids **15**, 2461 (2003).

[18] R. J. Stevens, M. Wilczek, and C. Meneveau, Large-eddy simulation study of the logarithmic law for second-and higher-order moments in turbulent wall-bounded flow, J. Fluid Mech. **757**, 888 (2014).

[19] A. Morales, M. Wächter, and J. Peinke, Characterization of wind turbulence by higher-order statistics, Wind Energy **15**, 391 (2012).

[20] C. Meneveau and I. Marusic, Generalized logarithmic law for high-order moments in turbulent boundary layers, J. Fluid Mech. **719**, R1 (2013).

[21] G. G. Katul, T. Banerjee, D. Cava, M. Germano, and A. Porporato, Generalized logarithmic scaling for high-order moments of the longitudinal velocity component explained by the random sweeping decorrelation hypothesis, Phys. Fluids **28**, 095104 (2016).

[22] H. Tennekes, Eulerian and lagrangian time microscales in isotropic turbulence, J. Fluid Mech. **67**, 561 (1975).

[23] G. I. Taylor, The spectrum of turbulence, Proc. R. Soc. Lond., A Math. Phys. Sci. **164**, 476 (1938).

[24] A. N. Kolmogorov, The local structure of turbulence in incompressible viscous fluid for very large Reynolds numbers, Proc. R. Soc. Lond., A Math. Phys. Sci. **434**, 9 (1991).

[25] J. A. Dutton and D. G. Deaven, Some observed properties of atmospheric turbulence, in *Statistical Models and Turbulence* (Springer, 1972) pp. 352–383.

[26] A. N. Kolmogorov, The local structure of turbulence in incompressible viscous fluid for very large Reynolds numbers, Cr Acad. Sci. URSS **30**, 301 (1941).

[27] C. Van Atta and J. Wyngaard, On higher-order spectra of turbulence, J. Fluid Mech. **72**, 673 (1975).

[28] G. G. Katul and C.-R. Chu, A theoretical and experimental investigation of energy-containing scales in the dynamic sublayer of boundary-layer flows, Bound.-Layer Meteorol. **86**, 279 (1998).

[29] T. Banerjee, D. Li, J.-Y. Juang, and G. Katul, A spectral budget model for the longitudinal turbulent velocity in the stable atmospheric surface layer, J. Atmos. Sci. **73**, 145 (2016).

[30] C. M. Tchen, On the spectrum of energy in turbulent shear flow, J. Res. Natl. Bur. Stand. **50**, 51 (1953).

[31] C. M. Tchen, Transport processes as foundations of the Heisenberg and Obukhoff theories of turbulence, Phys. Rev. **93**, 4 (1954).

[32] M. Chamecki and N. L. Dias, The local isotropy hypothesis and the turbulent kinetic energy dissipation rate in the atmospheric surface layer, Q. J. R. Meteorol. Soc. **130**, 2733 (2004).

[33] B. A. Kader and A. M. Yaglom, Spectra and correlation functions of surface layer atmospheric turbulence in unstable thermal stratification, in *Turbulence and Coherent Structures* (Springer, 1991) pp. 387–412.

[34] S. Pond, S. Smith, P. Hamblin, and R. Burling, Spectra of velocity and temperature fluctuations in the atmospheric boundary layer over the sea, J. Atmos. Sci. **23**, 376 (1966).

[35] P. S. Klebanoff, *Characteristics of turbulence in a boundary layer with zero pressure gradient*, Tech. Rep. (National Bureau of Standards, 1955).

[36] G. G. Katul, C. R. Chu, M. B. Parlange, J. D. Albertson, and T. A. Ortenburger, Low-wavenumber spectral characteristics of velocity and temperature in the atmospheric surface layer, J. Geophys. Res. Atmos. **100**, 14243 (1995).

[37] A. A. Praskovsky, E. B. Gledzer, M. Y. Karyakin, and Y. Zhou, The sweeping decorrelation hypothesis and energy–inertial scale interaction in high Reynolds number flows, J. Fluid Mech. **248**, 493 (1993).

[38] T. Morrison, M. Calaf, C. Higgins, S. Drake, A. Perelet, and E. Pardyjak, The impact of surface temperature heterogeneity on near-surface heat transport, Bound.-Layer Meteorol. (2021).

[39] J. C. Klewicki, J. F. Foss, and J. M. Wallace, High Reynolds number [$R_\theta = \mathrm{O}(10^6)$] boundary layer turbulence in the atmospheric surface layer above western Utah's salt flats, in *Flow at Ultra-High Reynolds and Rayleigh Numbers* (Springer, 1998) pp. 450–466.

[40] M. M. Metzger and J. C. Klewicki, A comparative study of near-wall turbulence in high and low Reynolds number boundary layers, Phys. Fluids **13**, 692 (2001).

[41] M. Vallikivi and A. J. Smits, Fabrication and characterization of a novel nanoscale thermal anemometry probe, J. Microelectromechanical Syst. **23**, 899 (2014).

[42] Y. Fan, G. Arwatz, T. W. Van Buren, D. E. Hoffman, and M. Hultmark, Nanoscale sensing devices for turbulence measurements, Exp. Fluids **56**, 138 (2015).

[43] G. Arwatz, Y. Fan, C. Bahri, and M. Hultmark, Development and characterization of a nano-scale temperature sensor (T-NSTAP) for turbulent temperature measurements, Meas. Sci. Technol. **26**, 035103 (2015).

[44] K. Y. Huang, C. E. Brunner, M. K. Fu, K. Kokmanian, T. J. Morrison, A. O. Perelet, M. Calaf, E. Pardyjak, and M. Hultmark, Investigation of the atmospheric surface layer using a novel high-resolution sensor array, Exp. Fluids **62**, 1 (2021).

[45] K. Y. Huang, G. G. Katul, and M. Hultmark, Velocity and temperature dissimilarity in the surface layer uncovered by the telegraph approximation, Bound.-Layer Meteorol. , 1 (2021).

[46] N. Hutchins, K. Chauhan, I. Marusic, J. Monty, and J. Klewicki, Towards reconciling the large-scale structure of turbulent boundary layers in the atmosphere and laboratory, Bound.-Layer Meteorol. **145**, 273 (2012).

[47] J. S. Bendat and A. G. Piersol, *Random data: analysis and measurement procedures* (John Wiley & Sons, 2011).

[48] M. Hultmark and A. J. Smits, Temperature corrections for constant temperature and constant current hot-wire anemometers, Meas. Sci. Technol. **21**, 105404 (2010).

[49] G. Katul, A. Konings, and A. Porporato, Mean velocity profile in a sheared and thermally stratified atmospheric boundary layer, Phys. Rev. Lett. **107**, 268502 (2011).

[50] S. Salesky, G. Katul, and M. Chamecki, Buoyancy effects on the integral lengthscales and mean velocity profile in atmospheric surface layer flows, Phys. Fluids **25**, 105101 (2013).
[51] J. C. Wyngaard, *Turbulence in the Atmosphere* (Cambridge University Press, 2010).
[52] S. Zilitinkevich, S. Tyuryakov, Y. I. Troitskaya, and E. Mareev, Theoretical models of the height of the atmospheric boundary layer and turbulent entrainment at its upper boundary, Izv. - Atmos. Ocean. Phys. **48**, 133 (2012).
[53] M. Raupach, Conditional statistics of reynolds stress in rough-wall and smooth-wall turbulent boundary layers, Journal of Fluid Mechanics **108**, 363 (1981).
[54] M. Heisel, G. G. Katul, M. Chamecki, and M. Guala, Velocity asymmetry and turbulent transport closure in smooth-and rough-wall boundary layers, Phys. Rev. Fluids **5**, 104605 (2020).
[55] H. Fernholz and P. Finleyt, The incompressible zero-pressure-gradient turbulent boundary layer: an assessment of the data, Prog. Aerosp. Sci. **32**, 245 (1996).
[56] T. Wei, P. Fife, J. Klewicki, and P. McMurtry, Properties of the mean momentum balance in turbulent boundary layer, pipe and channel flows, J. Fluid Mech. **522**, 303 (2005).
[57] M. Vallikivi, M. Hultmark, and A. J. Smits, Turbulent boundary layer statistics at very high Reynolds number, J. Fluid Mech. **779**, 371 (2015).
[58] G. G. Katul, C. Manes, A. Porporato, E. Bou-Zeid, and M. Chamecki, Bottlenecks in turbulent kinetic energy spectra predicted from structure function inflections using the von Kármán-Howarth equation, Physical Review E **92**, 033009 (2015).
[59] R. A. Antonia and M. R. Raupach, Spectral scaling in a high Reynolds number laboratory boundary layer, Bound.-Layer Meteorol. **65**, 289 (1993).